Journal of Nuclear Medicine, published on February 1, 2018 as doi:10.2967/jnumed.117.201632

Comparative *in-vitro* and *in-vivo* quantifications of pathological tau deposits and their association with neurodegeneration in tauopathy mouse models

Ruiqing Ni[1, 2], Bin Ji[1*], Maiko Ono[1], Naruhiko Sahara[1], Ming-Rong Zhang[1], Ichio Aoki[1], Agneta Nordberg[2], Tetsuya Suhara[1] and Makoto Higuchi[1]

[1]National Institute of Radiological Sciences, National Institutes for Quantum and Radiological Science and Technology, Chiba, Chiba 263-8555, Japan; [2]Division of Alzheimer Research Center, Department of Neurobiology, Care Sciences and Society, Karolinska Institutet, Stockholm 14157, Sweden

[*]Corresponding Author: Bin Ji, Ph. D.

Email: ji.bin@qst.go.jp,Tel: +81-43-206-3251, Fax: +81-43-253-0396, Address: National Institute of Radiological Sciences, National Institutes for Quantum and Radiological Science and Technology, 4-9-1, Anagawa, Inage-ku, Chiba-shi, Chiba 263-8555, Japan

First Author Information: Fellow. *Address/phone/fax* as above; ruiqing.ni@ki.se

Word count: 4099

Running title: Tau imaging in Alzheimer tauopathy mice

Financial support: This work was supported in part by Brain/MINDS (Brain Mapping by Integrated Neurotechnologies for Disease Studies) to M. H. (15653129), Research and Development Grant for Dementia (16768966) to M. H. and COI (Center of Innovation) Stream for MRI devices to I. A., and from the Japan Agency for Medical Research and Development and Grants-in-Aid for Scientific Research to B. J. (15K09979) and M. H. (16678815) and Postdoctoral Fellowship to R. N. (PE15760) from the Japan Society for the Promotion of Science.

Abstract:

Fibrillary tau aggregates in Alzheimer's disease (AD) and allied neurodegenerative disorders have been visualized *in-vivo* by positron emission tomography (PET), while mechanistic links between PET-detectable tau deposits and neurotoxicity remain elusive. Here, we took advantage of transgenic mouse models of tauopathies to evaluate associations between PET and postmortem measures of tau probe binding and their relation to neuronal loss.

Methods: PET with a tau probe, ^{11}C-PBB3 (2-((1E,3E)-4-(6-(^{11}C-methylamino)pyridine-3-yl)buta-1,3-dienyl)benzo[d]thiazol-6-ol), and volumetric magnetic resonance imaging (MRI) were performed for rTg4510 and non-transgenic mice. Binding of ^{11}C-PBB3 and its blockade by another tau binding compound, AV-1451 (-(6-fluoropyridine-3-yl)-5H-pyrido[4,3-b]indole), in homogenized brains of tauopathy patients and rTg4510 and PS19 mice were quantified, and PBB3-positive and phosphorylated tau lesions in sectioned brains of these mice were assessed.

Results: *In-vivo* ^{11}C-PBB3 binding to the rTg4510 neocortex/hippocampus was increased relative to controls, and was correlated with local atrophy. *In-vitro* ^{11}C-PBB3 binding in the neocortex/hippocampus was also well correlated with *in-vivo* radioligand binding and regional atrophy in the same individual rTg4510 mice. By contrast, *in-vitro* ^{11}C-PBB3 binding was elevated in the brainstem but not hippocampus of PS19 mice, despite a pronounced loss of neurons in the hippocampus rather than brainstem. Finally, PBB3 and AV-1451 showed similar binding properties between mouse models and tauopathy patients.

Conclusions: The present findings support the distinct utilities of ^{11}C-PBB3-PET along with MRI of rTg4510 and PS19 mice for quantitatively pursuing mechanisms connecting PET-detectable and

PET-undetectable tau aggregations to neuronal death, which recapitulate two different modes of tau-provoked neurotoxicity.

Keywords: Tauopathy; Transgenic mouse model; Small-animal PET; Volumetric MRI; Radioligand binding

INTRODUCTION

Deposition of pathological tau fibrils is characteristic of AD and related non-AD neurodegenerative disorders as exemplified by frontotemporal lobar degeneration (FTLD) (*1*). Normally functioning tau proteins are constituents of axonal cytoskeletons in neurons, and the self-assembly of tau molecules in a diseased condition gives rise to disruption of the axonal framework along with neurotoxicity induced by misfolded tau species (*1,2*). In line with this mechanistic view, tau abnormalities are known to be tightly associated with neurodegeneration and the emergence of clinical symptoms (*3,4*) providing a rationale for anti-tau treatments to modify the disease process (*5*). For the purpose of establishing etiological, diagnostic and therapeutic assessments of tau pathologies in living subjects, there have been growing demands for the visualization of tau fibrils in a non-invasive manner.

In-vivo PET of tau lesions has recently been enabled by the development of small-molecule imaging agents selectively binding to the β-pleated sheet structure in tau filaments (*6*). Several tau PET probes, including ^{11}C-PBB3 (*7*), ^{18}F-THK5117 (*8*), ^{18}F-THK5351 (*9*) and ^{18}F-AV-1451 (also known as ^{18}F-T807 or ^{18}F-flortaucepir) (*10-12*), have been applied to human subjects across the AD spectrum, and have offered neuroimaging-based staging of tau pathologies. In these individuals, the distribution of PET-detectable tau deposits was reported to agree with the topography of brain atrophy and manifestation of focal symptoms (*7,9,12*), implicating the tau aggregation in the local neuronal deteriorations. In the meantime, it still remains elusive whether tau deposits in FTLD are sensitively detectable by these PET probes to examine links between the localization of tau pathologies and clinical phenotypes (*13-17*). It is noteworthy that tau proteins

are composed of six isoforms classified into 4-repeat and 3-repeat species, and the composition of tau isoforms differs among diverse tauopathies (*1,2*). Indeed, AD-type tau fibrils are constituted by all six isoforms, in contrast to the exclusive assembly of 4-repeat tau (4RT) isoforms into fibrils in a subgroups of FTLD, such as progressive supranuclear palsy (PSP) and corticobasal degeneration (*1,2*). These distinct tau fibril species are ultra-structurally identified as paired helical filaments (PHFs) in AD and straight filaments (SFs) in 4-repeat tauopathies (*18,19*), and such conformational variations may affect the reactivity of tau fibrils with PET probes (*13*). In fact, binding of [^{11}C]PBB3 in the PSP motor cortex is not blocked by AV-1451 in contrast with a partial blockade of [^{11}C]PBB3 binding by AV-1451 in the AD temporal cortex. The binding characteristics of these ligands can accordingly be utilized for discrimination between 'AD-like' and 'PSP-like' tau aggregates in human and mouse brain tissues.

In the non-clinical development of ^{11}C-PBB3 (*7*), we utilized mice transgenic (Tg) for a human 4RT isoform with the P301L and P301S mutations, termed rTg4510 (*20*) and PS19 (*21*) lines, respectively. *In-vivo* PET and *ex-vivo* autoradiographic, and *in-vivo* and *ex-vivo* fluorescence imaging of these animals provided significant information on the kinetics and detectability of tau deposits in the living brain by a candidate imaging agent (*7*). However, it still remains unclear whether preclinical investigation using rTg4510 and PS19 combined with ^{11}C-PBB3-PET could provide useful information on imaging-pathological relationships as in clinical PET study or potentially contribute for quantitatively understanding mechanisms connecting PET-detectable and PET-undetectable tau aggregations to neuronal death. It should also be noted that the radioligand binding in small-animal PET assays could be underestimated in small anatomical structures due to

partial volume effects, and could be overestimated in surface brain areas as a consequence of radioactivity spill-in from extracranial tissues. PET measures should accordingly be validated with reference to postmortemly acquired binding estimates in the same individuals.

In order to address these issues, we conducted ^{11}C-PBB3-PET and volumetric MRI of rTg4510 mice, followed by postmortem assessments of the brains from the same animals, and assessed whether *in-vivo* PET signals reflect the amount of specific ^{11}C-PBB3 binding and phosphorylated tau deposits. Associations of these binding estimates with cerebral atrophy determined by MRI were also analyzed to demonstrate the ability of ^{11}C-PBB3-PET to quantify tau species tightly linked to the neurotoxicity. Similarly, *in-vitro* binding assays were applied to brain tissues collected from PS19 mice to clarify if toxicity-related tau assemblies can be captured by ^{11}C-PBB3 across different tauopathy models. Finally, *in-vitro* binding of ^{11}C-PBB3 versus AV-1451 in rTg4510 and PS19 mouse samples was compared with those of AD and PSP tissues for examining the translatability of the probe binding data in mouse models to AD and 4-repeat tauopathies. Assessments of the competition between ^{11}C-PBB3 and AV-1451 binding in various brain tissues would also provide information on the presence of common off-target binding sites for these two compounds.

MATERIAL AND METHODS

Ethics Statement

The mice studied here were maintained and handled in accordance with National Research Council's Guide for the Care and Use of Laboratory Animals and our institutional guidelines.

Protocols for the present animal experiments were approved by the Animal Ethics Committees of the National Institute of Radiological Sciences, National Institutes for Quantum and Radiological Science and Technology. The research using autopsied human samples was approved by the Ethics Committee of National Institute of Radiological Sciences.

Reagents and Antibody

PBB3 and a desmethyl precursor for radiosynthesis of ^{11}C-PBB3 were obtained from Nard Institute (Kobe, Japan). AV-1451 was in-house synthesized according to a previous report (US 2012/0302755 A1). BTA-1, clorgyline, and selegiline (also known as deprenyl) were purchased from Sigma-Aldrich (St. Louis, MO, USA). AT8, a mouse monoclonal antibody against human tau phosphorylated at Ser202 and Thr205, was purchased from Endogen/Thermo Fisher Scientific (Waltham, MA, USA).

Animal Models

Two mouse models, PS19 and rTg4510 mice, were used in the present study. The detailed information of these mouse models was shown in **SUPPLEMENTARY INFORMATION**. A workflow of *in-vivo* PET and MRI and *in-vitro* binding assays with rTg4510 and non-Tg mice is shown in Supplemental Figure 1 (SFig. 1).

Radiosynthesis and Small-animal PET Imaging

Radiosynthesis of ^{11}C-PBB3 was performed as described (*7*), and the resulting radiochemical

purity was > 90 %. The molar activity of ^{11}C-PBB3 was 78-93.1 GBq/μmol at the end of synthesis. PET scans were performed by microPET Focus 220 animal scanner (Siemens Medical Solutions, Malvern, PA, USA) as described (*22*). At 7-10 months of age, rTg4510 mice (n = 5, body weight: 23.6 ± 0.8 g) and age-matched non-Tg mice (n = 7, body weight: 29.1 ± 1.5 g) were intravenously injected with ^{11}C-PBB3 (18.2-23.4 MBq/mouse; 20.76 ± 2.21 MBq for non-Tg and 21.24 ± 1.24 MBq for Tg mice). Volumes of interest (VOIs) were placed on multiple anatomical structures, including the neocortex, whole hippocampus, cerebellum (Fig. 1A and SFig. 2). Tracer uptake in each VOI was estimated as a percentage of injected-dose-per-tissue-volume (%ID/mL), which was uncorrected for body weights of animals, since changes of body weights during aging may not be necessarily proportional to alterations of brain weights. Non-displaceable binding potential (BP_{ND}) for ^{11}C-PBB3 binding in these VOIs, which is not influenced by either body or brain weights, was quantified with PMOD based on a simplified reference tissue model using the cerebellum as a reference region lacking tau deposits. The detailed information of the experiments was shown in **SUPPLEMENTARY INFORMATION**.

MRI of Mouse Brains, *In-vitro* ^{11}C-PBB3 Binding Assays and Immunohistochemical and Histochemical Analyses

The detailed information of the experiments was shown in **SUPPLEMENTARY INFORMATION**.

Statistics

Statistical analyses for comparison of mouse genotype groups were performed by unpaired *t*-test using GraphPad Prism 5.0. The difference between groups was considered significant at p value < 0.05. All error bars in the figures are expressed as standard error of the mean (S.E.M).

RESULTS

Increased *in-vivo* ^{11}C-PBB3 Binding Correlates with Brain Atrophy in rTg4510 Mice

Images of ^{11}C-PBB3-PET and structural MRI demonstrated overtly increased radioactivity retention and decreased volume in the either neocortex or hippocampus of rTg4510 mice compared to age-matched non-Tg mice (Fig. 1A). Time-activity curves also indicated increased ^{11}C-PBB3 retention in the neocortex/hippocampus relative to the cerebellum of rTg451 mice, while no overt regional difference in radioligand retention was observed in non-Tg mice (Fig. 1B). BP_{ND} for ^{11}C-PBB3 was significantly increased by 3-5 fold in the neocortex and hippocampus of rTg4510 compared to non-Tg mice (Fig. 1C). This change was concurrent with marked reductions of the neocortical (approximately 33 %) and hippocampal (approximately 38 %) volumes in rTg4510 mice relative to non-Tg mice (Fig. 1C). Indeed, intimate correlations between ^{11}C-PBB3 BP_{ND} and the volume of either neocortex or hippocampus were found in an analysis of combined Tg and non-Tg mice. This approach was made by conceiving non-transgenic mice to be animals at 'stage 0' of the tau pathology. In an assessment of the transgenics only, BP_{ND} values were still significantly correlated with local volumes in the hippocampus, and showed a tendency to correlate with each other in the neocortex, despite a small sample size (Fig. 1D).

Postmortem Assays of Tau Pathologies in rTg4510 and PS19 Mice

Abundant neuronal inclusions fluorescently stained with PBB3 and immunolabeled with AT8 were observed in the neocortex and hippocampus but not in the cerebellum (data not shown) of 7-10-month-old rTg4510 mice. Similarly, accumulation of PBB3- and AT8-positive tau deposits was detected in the brainstem of 13-month-old PS19 mice. There was a lack of intense fluorescence labeling with PBB3 in the hippocampus of these PS19 mice despite abundant immunostaining with AT8 (Fig. 2A). *In-vitro* ^{11}C-PBB3 binding was also increased in the neocortex/hippocampus of 7-10-month-old rTg4510 mice and mixed brainstem/spinal cord tissues of 13-month-old PS19 mice compared to corresponding non-Tg littermates, while ^{11}C-PBB3 binding in the mixed neocortex/hippocampus tissues of these PS19 was unchanged relative to age-matched non-Tg mice (Fig. 2B). *In-vitro* ^{11}C-PBB3 binding showed good correlation with both *in-vivo* ^{11}C-PBB3 binding and volume reduction in the neocortex/hippocampus of rTg4510 and non-Tg mice (Fig. 2C, D).

Characteristics of Tau Fibrils in Mouse Models versus AD and PSP Based on Binding of PBB3 and AV-1451

We assumed that conformational features of tau fibrils in the brain could be probed by their reactivity with different ligands. Following this rationale, ^{11}C-PBB3 binding in homogenized frontal cortical tissues of an AD patient with abundant amyloid plaques and neurofibrillary tangles in the frontal cortex (SFig. 3) was measured under a homologous blockade by non-labeled PBB3 and a heterologous blockade by AV-1451 or BTA-1. The homologous blocking of ^{11}C-PBB3 binding by non-labeled PBB3 indicated the presence of high- and low-affinity binding components

for this ligand with Ki (= K_D) values of 3.9 nM and 246.6 nM, respectively (Fig. 3A). The heterologous blockade of ^{11}C-PBB3 binding by BTA-1, which is more selective for Aβ versus tau filaments, was well described by a one-site model, with Ki value of 79.0 nM (Fig. 3A). According to this inhibition curve, BTA-1 at a concentration below 50 nM in the AD brain, which could reflect its high-affinity binding to Aβ aggregates, minimally blocked the specific ^{11}C-PBB3 binding. AV-1451 displaced 30-40 % of ^{11}C-PBB3 binding at maximum in the AD tissue (Fig. 3A). This blockade was described by a one-site model with Ki value of 89.6 nM, which was approximately 50-fold weaker than the homologous blockade by non-labeled PBB3. In the PSP basal ganglia tissue, a one-site model indicated high-affinity binding of ^{11}C-PBB3 to tau deposits with a Ki (=K_D) value of 2 nM, and this was barely blocked by AV-1451 even at a high concentration (Fig. 3B).

Likewise, ^{11}C-PBB3 exhibited high-affinity binding to tau deposits in the neocortex/hippocampus of rTg4510 mice (Fig. 3C) and the brainstem/spinal cord of PS19 mice (Fig. 3D) with Ki (= K_D) values of 1.8 nM and 1.3 nM, respectively, and this radioligand binding was only minimally inhibited by AV-1451 at high concentrations (Fig. 3C, D).

The lack of competitions between ^{11}C-PBB3 and AV-1451 bindings in PSP and Tg mouse brain samples supports the view that ^{11}C-PBB3 does not react with probable off-target binding components for AV-1451, including monoamine oxidase A (MAO-A) and iron-containing deposits (*23*). Finally, minimal displacements of ^{11}C-PBB3 binding were observed in the presence of MAO-A inhibitor, clorgyline, or monoamine oxidase B (MAO-B) inhibitor, selegiline, in homogenates from the AD frontal cortex even at high concentrations (Fig. 3E), suggesting that ^{11}C-PBB3 can barely react with off-target binding sites on monoamine oxidases.

DISCUSSION

The current findings provide *in-vitro* and *in-vivo* evidence for the conformational homology between pathological tau assemblies in human tauopathies and mouse models as probed by ^{11}C-PBB3. Binding assays of ^{11}C-PBB3 in comparison with AV-1451 have demonstrated that tau fibrils in Tg mice overexpressing a single 4RT isoform particularly resemble SFs in 4RT disorders represented by PSP. These indications are supportive of the notion that PET imaging of the model animals along with postmortem investigations with ^{11}C-PBB3 offers assay systems seamlessly linking non-clinical and clinical evaluations of candidates for therapeutic and diagnostic agents targeting the tau depositions. To further justify the use of the non-clinical ^{11}C-PBB3-PET system with rTg4510 and PS19 mice, a more extensive *in-vitro* analysis of the relevance between radioligand binding profiles in Tg mouse and human tissues will be required with a larger sample size and different brain areas. There might be regional and inter-individual differences in the conformational properties and neurotoxicity of pathological tau assemblies within a single disease, although the present data using the AD frontal cortex and PSP basal ganglia (Fig. 3C, 3D) was in agreement with previous findings in different tangle-rich brain regions of patients with these illnesses (*13*).

As illustrated in Fig. 3, ^{11}C-PBB3 is capable of binding to tau deposits in the PSP and Tg mouse brain tissues with a high affinity, and this binding was not blocked by AV-1451 even at a high concentration above 100 nM. This observation demonstrates the resemblance of SFs composed of 4RTs in PSP and Tg models, raising the possibility that PET scans of these mice will facilitate the development of a probe for high-contrast imaging of tau lesions in PSP and allied 4-

repeat tauopathies. Such new imaging agents would be generated on the basis of the PBB3 backbone structure, in light of the current data.

In the AD brain, Aβ and tau aggregates share a common β-pleated sheet structure that is in principle reactive with diverse β-sheet ligands, but our present and previous results (*7*,*13*) suggest that ^{11}C-PBB3 at a concentration below 10 nM, which is comparable to the radioligand concentration in the brain achievable in a clinical PET study, primarily react with tau versus Aβ deposits in the brains of AD patients. Indeed, the peak concentration of ^{11}C-PBB3 is conceived to be 10 nM or below in human and mouse PET studies, according to the current and previous (*7*) data, and is therefore considered to be close to the concentration of ^{11}C-PBB3 (i. e. 5 nM) used for the current homogenate biding assays. As BTA-1 binds to Aβ aggregates with high affinity, the blockade of specific ^{11}C-PBB3 binding in AD tissues by 1-50 nM of BTA-1 should reflect the binding of ^{11}C-PBB3 to Aβ deposits, which was found to be minimal (Fig. 3A). Meanwhile, the heterologous blockade by BTA-1 at high concentrations above 100 nM is likely to primarily stem from the low-affinity binding of BTA-1 to tau fibrils. This finding is in agreement with previous autoradiographic binding measurements indicating that ^{11}C-PBB3 at a concentration below 10 nM mostly reacts with high-affinity components on tau fibrils relative to low-affinity elements on Aβ fibrils in AD brain sections. Moreover, the affinities of ^{11}C-PBB3 for tau in the brains of AD patient and Tg mouse were close to each other, validating the use of these animals for non-clinical characterization of ^{11}C-PBB3 and *in-vivo* screening of PBB derivatives for imaging AD-type tau pathologies. Notwithstanding these supportive evidences, the property of ^{11}C-PBB3 and resemblance between AD and transgenic mouse tau fibrils will need to be further examined by

increasing the sample size of AD tissues.

It is noteworthy that ^{11}C-PBB3 binding in AD brain homogenates was only partially blocked by AV-1451 with a Ki value of 89.6 nM (Fig. 3A), which is consistent with our previous report (*13*). Since specific binding of 5 nM ^{11}C-PBB3 was barely inhibited barely by 1-50 nM AV-1451, PBB3 and AV-1451 may not share high-affinity binding components in AD tau filaments. In addition, the high-affinity binding of 5 nM ^{11}C-PBB3 was only modestly blocked by AV-1451 at high concentrations (Fig. 3A). Hence, ^{11}C-PBB3 and ^{18}F-AV-1451 in living AD patients may detect different tau species that differentially contribute to neurotoxicity as implied by a previous *in-vitro* assessment (*13*), and this probability will be examined by a head-to-head comparison of these two radioligands in the same human subjects.

The present work also indicates an intimate correlation between *in-vivo* and *in-vitro* binding of ^{11}C-PBB3 in the same rTg4510 mice at 7-10-months of age. We defined PET VOIs in a subportion of the neocortex to circumvent technical issues of radioactivity spill-in and partial volume effects stemming from small volumes of the mouse brain regions, enabling quantification of the radioligand binding reflecting the amount of binding components. Because we observed a marked colocalization of PBB3 fluorescence labeling and AT8 immunostaining in the brain sections derived from these mice, *in-vivo* ^{11}C-PBB3-PET is presumed to be able to robustly quantify insoluble tau aggregates constituted of phosphorylated tau molecules. Meanwhile, there still remains a possibility of inaccurate measurements of the radioligand binding caused by insufficient volumes of target VOIs particularly in mice with severe pathologies, highlighting the need for further technical considerations in small-animal PET imaging.

According to the correlation between local brain atrophy and *in-vivo* ^{11}C-PBB3 binding in rTg4510 mice, neurons in the brains of these animals may die mainly at a pathological stage characterized by the accumulation of PBB3-labeled inclusions, and our previous data also demonstrates that neuronal loss is less prominent in the absence of PBB3 positivity notwithstanding the high abundance of tau oligomers (*24*), suggesting a potential role of PBB3-positive inclusions in the advancement of the neurotoxicity. In the meantime, extracellular tau deposits dubbed ghost tangles were not found in our histochemical and immunohistochemical analyses of the brain sections collected from rTg4510 mice. This implies death of tangle-bearing neurons followed by immediate elimination of tau aggregates and/or loss of tangle-negative neurons due to neurotoxicity of relatively immature tau assemblies. To examine these possibilities, longitudinal PET and intravital microscopic imaging experiments need to be conducted and are currently underway. In PET scans of patients with AD and/or mild cognitive impairment (*7*,*25*), an increase of ^{11}C-PBB3 binding has been reported to be correlated with either local atrophy or cognitive performance, suggesting that the neuronal loss in these diseases is mediated by molecular mechanisms linked to PBB3-positive tau fibrils similar to those in rTg4510 mice.

In contrast to the pathologies in rTg4510 mice, AT8-immunoreactive tau deposits in the neocortex/hippocampus of PS19 mice barely reacted with PBB3. In the meantime, a pronounced increase of tau lesions doubly positive for AT8 and PBB3 occurred in the brainstem and spinal cord of the PS19 strain. As regional atrophy was severe in the neocortex/hippocampus and modest in the brainstem and spinal cord of these animals (*7*,*21*), the concurrence of PBB3-negative, AT8-positive inclusions with loss of neurons and absence of ghost tangles in the hippocampus of PS19

mice might indicate the neurotoxicity of PBB3-negative tau assemblies, or immediate elimination of neurons bearing PBB3-positive tau tangles. Furthermore, the PBB3 negativity in the PS19 hippocampus may be attributable to the formation of region-specific conformers and posttranslational modifications of tau molecules, leading to the loss of their reactivity with PBB3. The reactivity of different PET probes with tauopathy mouse models in addition to rTg4510 and PS19 mice is also of significant interest. A previous PET study documented that another tau PET ligand, ^{18}F-THK5117, enabled quantification of tau deposits in two different tau Tg mouse models (*26*), while the relationships between tau PET signals and regional atrophy in these strains remain undetermined. Furthermore, it should be noted that THK5117 and related quinoline derivatives may cross-react with MAO-B (*27*), which is abundantly present in activated astrocytes, while ^{18}F-AV-1451 may bind to MAO-A (*23*). Our *in-vitro* assays indicate that ^{11}C-PBB3 binding in AD brain homogenates does not compete with inhibitors of either MAO-A or MAO-B, and therefore ^{11}C-PBB3-PET signals in human and mouse brains are considered to reflect tau lesions, not other neuropathological events such as astrogliosis enriched with MAO-B.

CONCLUSION

Our PET and MRI analyses of tau Tg mice in conjunction with postmortem radiochemical, histochemical and immunohistochemical assays have proven the applicability of ^{11}C-PBB3 to the research on neurodegenerative tauopathies reciprocally linking non-clinical and clinical evidences. The findings obtained here have also revealed the distinct utilities of rTg4510 and PS19 models for assessing putative etiological pathways triggered by either PBB3-positive or PBB3-negative

tau multimers.

ACKNOWLEDGEMENTS

The authors thank Prof. John Q. Trojanowski and Prof. Virginia M.-Y. Lee (Center for Neurodegenerative Disease Research, University of Pennsylvania) for kindly providing human brain tissues and PS19 mice; Prof. Jada Lewis of the University of Florida for supporting analyses of rTg4510 mice; Takeharu Minamihisamatsu, Shoko Uchida, Sayuri Sasaki, Sayaka Shibata, Nobuhiro Nitta and Yoshikazu Ozawa for their technical assistance.

Disclosure: Nothing to declare

REFERENCES:

1. Lee VM, Goedert M, Trojanowski JQ. Neurodegenerative tauopathies. *Annu Rev Neurosci.* 2001;24:1121-1159.

2. Higuchi M, Lee VM, Trojanowski JQ. Tau and axonopathy in neurodegenerative disorders. *Neuromolecular Med.* 2002;2:131-150.

3. Murray ME, Graff-Radford NR, Ross OA, Petersen RC, Duara R, Dickson DW. Neuropathologically defined subtypes of Alzheimer's disease with distinct clinical characteristics: a retrospective study. *Lancet Neurol.* 2011;10:785-796.

4. Nelson PT, Alafuzoff I, Bigio EH, et al. Correlation of Alzheimer disease neuropathologic changes with cognitive status: a review of the literature. *J Neuropathol Exp Neurol.* 2012;71:362-381.

5. Khanna MR, Kovalevich J, Lee VM, Trojanowski JQ, Brunden KR. Therapeutic strategies for the treatment of tauopathies: Hopes and challenges. *Alzheimers Dement.* 2016;12:1051-1065.

6. Villemagne VL, Fodero-Tavoletti MT, Masters CL, Rowe CC. Tau imaging: early progress and future directions. *Lancet Neurol.* 2015;14:114-124.

7. Maruyama M, Shimada H, Suhara T, et al. Imaging of tau pathology in a tauopathy mouse model and in Alzheimer patients compared to normal controls. *Neuron.* 2013;79:1094-1108.

8. Okamura N, Furumoto S, Harada R, et al. Novel 18F-labeled arylquinoline derivatives for noninvasive imaging of tau pathology in Alzheimer disease. *J Nucl Med.* 2013;54:1420-1427.

9. Harada R, Okamura N, Furumoto S, et al. 18F-THK5351: A Novel PET Radiotracer for Imaging Neurofibrillary Pathology in Alzheimer Disease. *J Nucl Med.* 2016;57:208-214.

10. Chien DT, Bahri S, Szardenings AK, et al. Early clinical PET imaging results with the novel PHF-tau radioligand [F-18]-T807. *J Alzheimers Dis.* 2013;34:457-468.

11. Chien DT, Szardenings AK, Bahri S, et al. Early clinical PET imaging results with the novel PHF-tau radioligand [F18]-T808. *J Alzheimers Dis.* 2014;38:171-184.

12. Johnson KA, Schultz A, Betensky RA, et al. Tau positron emission tomographic imaging in aging and early Alzheimer disease. *Ann Neurol.* 2016;79:110-119.

13. Ono M, Sahara N, Kumata K, et al. Distinct binding of PET ligands PBB3 and AV-1451 to tau fibril strains in neurodegenerative tauopathies. *Brain.* 2017.

14. Marquie M, Normandin MD, Meltzer AC, et al. Pathological correlations of [F-18]-AV-1451 imaging in non-alzheimer tauopathies. *Ann Neurol.* 2017;81:117-128.

15. Hammes J, Bischof GN, Giehl K, et al. Elevated in vivo [18F]-AV-1451 uptake in a patient with progressive supranuclear palsy. *Mov Disord.* 2017;32:170-171.

16. Coakeley S, Cho SS, Koshimori Y, et al. Positron emission tomography imaging of tau pathology in progressive supranuclear palsy. *J Cereb Blood Flow Metab.* 2016:271678X16683695.

17. Ishiki A, Harada R, Okamura N, et al. Tau imaging with [18 F]THK-5351 in progressive supranuclear palsy. *Eur J Neurol.* 2017;24:130-136.

18. Bibow S, Mukrasch MD, Chinnathambi S, et al. The dynamic structure of filamentous tau. *Angew Chem Int Ed Engl.* 2011;50:11520-11524.

19. Murray ME, Kouri N, Lin WL, Jack CR, Jr., Dickson DW, Vemuri P. Clinicopathologic assessment and imaging of tauopathies in neurodegenerative dementias. *Alzheimers Res Ther.* 2014;6:1.

20. Santacruz K, Lewis J, Spires T, et al. Tau suppression in a neurodegenerative mouse model improves memory function. *Science.* 2005;309:476-481.

21. Yoshiyama Y, Higuchi M, Zhang B, et al. Synapse loss and microglial activation precede tangles in a P301S tauopathy mouse model. *Neuron.* 2007;53:337-351.

22. Ji B, Maeda J, Sawada M, et al. Imaging of peripheral benzodiazepine receptor expression as biomarkers of detrimental versus beneficial glial responses in mouse models of Alzheimer's and other CNS pathologies. *J Neurosci.* 2008;28:12255-12267.

23. Marquie M, Normandin MD, Vanderburg CR, et al. Validating novel tau positron emission tomography tracer [F-18]-AV-1451 (T807) on postmortem brain tissue. *Ann Neurol.* 2015;78:787-800.

24. Sahara N, Ren Y, Ward S, Binder LI, Suhara T, Higuchi M. Tau oligomers as potential targets for early diagnosis of tauopathy. *J Alzheimers Dis.* 2014;40 Suppl 1:S91-96.

25. Shimada H, Kitamura S, Shinotoh H, et al. Association between Abeta and tau accumulations and their influence on clinical features in aging and Alzheimer's disease spectrum brains: A [11C]PBB3-PET study. *Alzheimers Dement (Amst).* 2017;6:11-20.

26. Brendel M, Jaworska A, Probst F, et al. Small-Animal PET Imaging of Tau Pathology with 18F-THK5117 in 2 Transgenic Mouse Models. *J Nucl Med.* 2016;57:792-798.

27. Ng KP, Pascoal TA, Mathotaarachchi S, et al. Monoamine oxidase B inhibitor, selegiline, reduces 18F-THK5351 uptake in the human brain. *Alzheimers Res Ther.* 2017;9:25.

Legends to figures

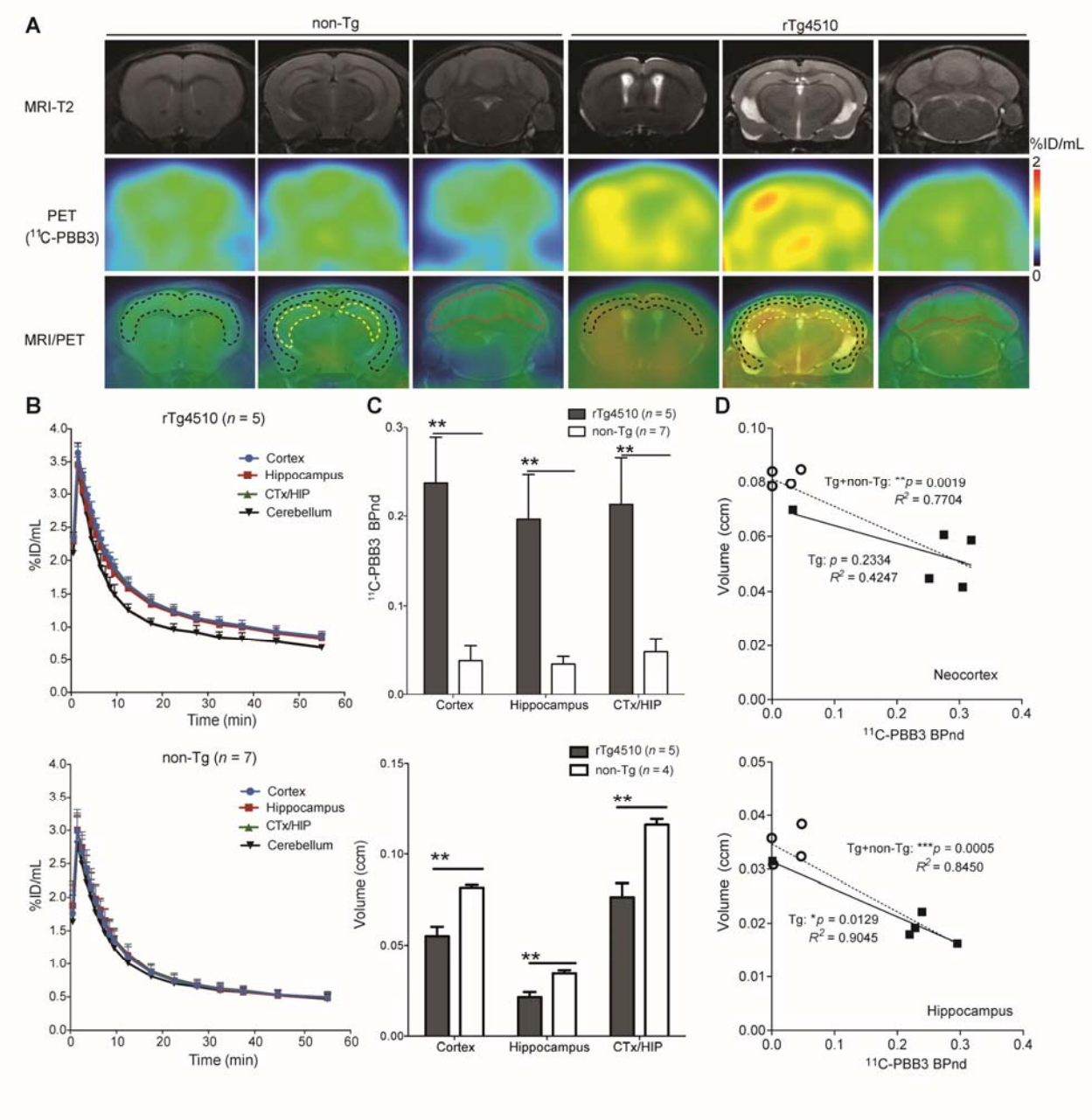

Figure 1 Correlations of PBB3-positive tau deposits with neocortical/hippocampal atrophy in the rTg4510 mouse brain. (A) Representative T_2-weighted MRI (upper row), PET (middle row) and merged PET/MRI (lower row) images of coronal mouse brain sections containing the neocortical, hippocampal and cerebellar VOIs (outlined by black, yellow and red dashed lines,

respectively) of 9-month-old non-Tg and rTg4510 mice. The PET images were generated from averaged dynamic data at 30-60 min after the injection of ^{11}C-PBB3. (B) Time-activity curves for ^{11}C-PBB3 in different brain regions of rTg4510 (upper, n = 5) and age-matched non-Tg (lower, n = 7) mice at 7-10 months of age. (C) ^{11}C-PBB3 binding potential (BP_{ND}) in each VOI was calculated by simplified reference tissue model with the cerebellum as reference tissue (upper, data from panel B). Brain volume was measured by using structural MRI data (lower). The BP_{ND} of CTX/HIP (neocortex and hippocampus) was also calculated. Statistical analysis showed significant increase in ^{11}C-PBB3 BP_{ND} and decrease in the volumes of the neocortex and the hippocampus of rTg4510 mice compared to non-Tg littermates (**, $p < 0.01$ by unpaired t-test). (D) Correlations between ^{11}C-PBB3 BP_{ND} and volumes of the neocortex (upper) and hippocampus (lower) in rTg4510 (filled squares) and non-Tg mice (open circles). Results of statistical tests for the correlations in a combined Tg and non-Tg group (Tg + non-Tg) and Tg mice only are displayed (*, p <0.05; **, p <0.01; and ***, p <0.001 by t-test; and R, Pearson's correlation coefficient). Dotted and solid lines represent regressions in the Tg + non-Tg group and Tg mice only, respectively.

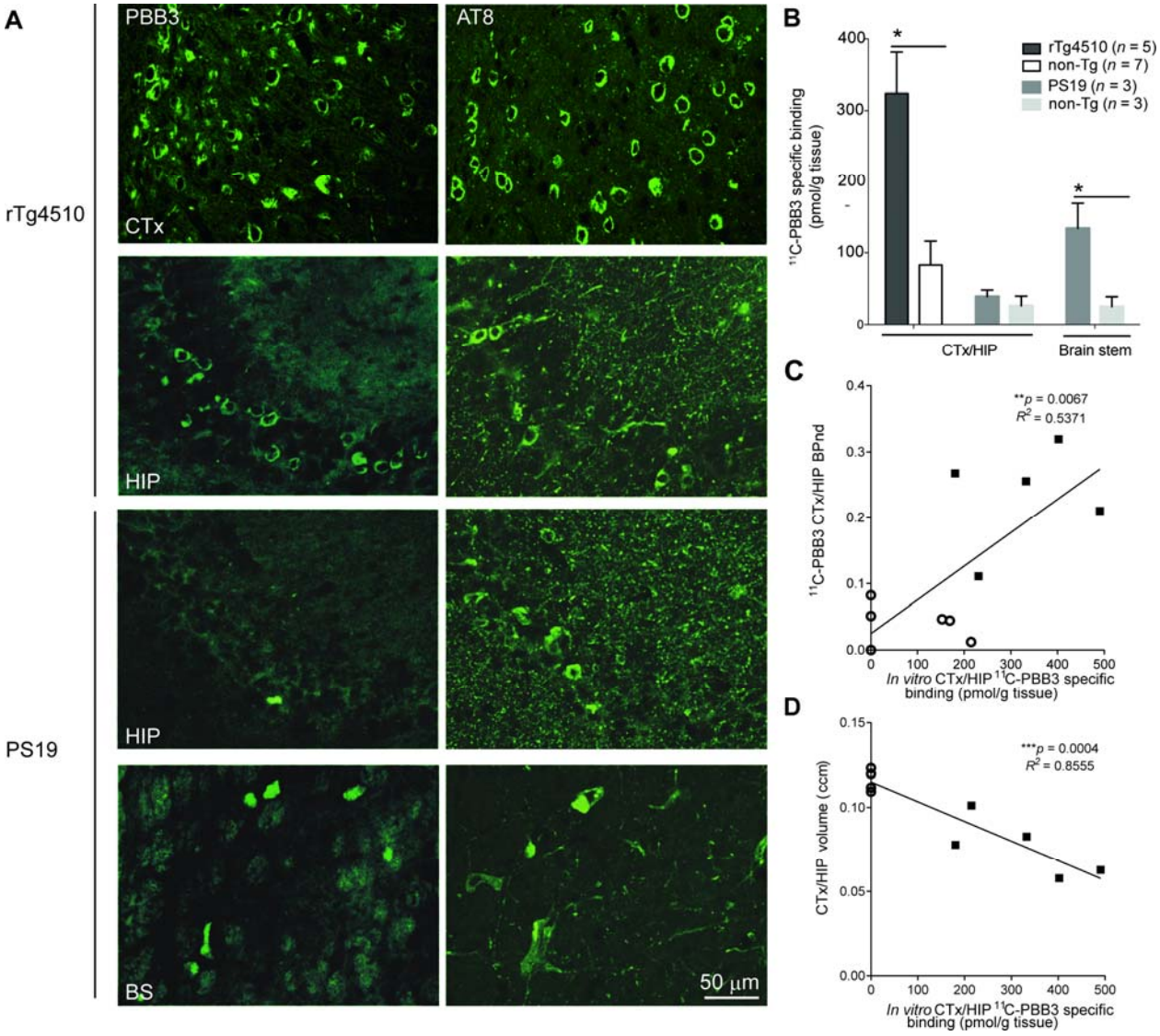

Figure 2 Comparisons of *in-vitro* ^{11}C-PBB3 binding and histochemical and immunohistochemical findings in the brains of rTg4510 and PS19 mice. (A) Representative images of PBB3-positive tau deposits and phosphorylated tau (AT8) were acquired in various brain regions (CT, cortex; HIP, hippocampus; BS, brainstem) in 9-month-old rTg4510 and 13-month-old PS19 mice. (B) Specific binding of ^{11}C-PBB3 (5 nM) was increased in the CTX/HIP of rTg4510 mice and in the brainstem of PS19 mice compared to non-Tg littermates (*, $p < 0.05$ by unpaired *t*-test). No significant difference in ^{11}C-PBB3 binding was observed between the

CTX/HIP tissues of PS19 mice and non-Tg littermates. (C, D) There were significant correlations of *in-vitro* ^{11}C-PBB3 binding with *in-vivo* BP_{ND} (C) and the regional volumes (D) in the CTX/HIP of rTg4510 (filled square) and non-Tg (open circles) mice.

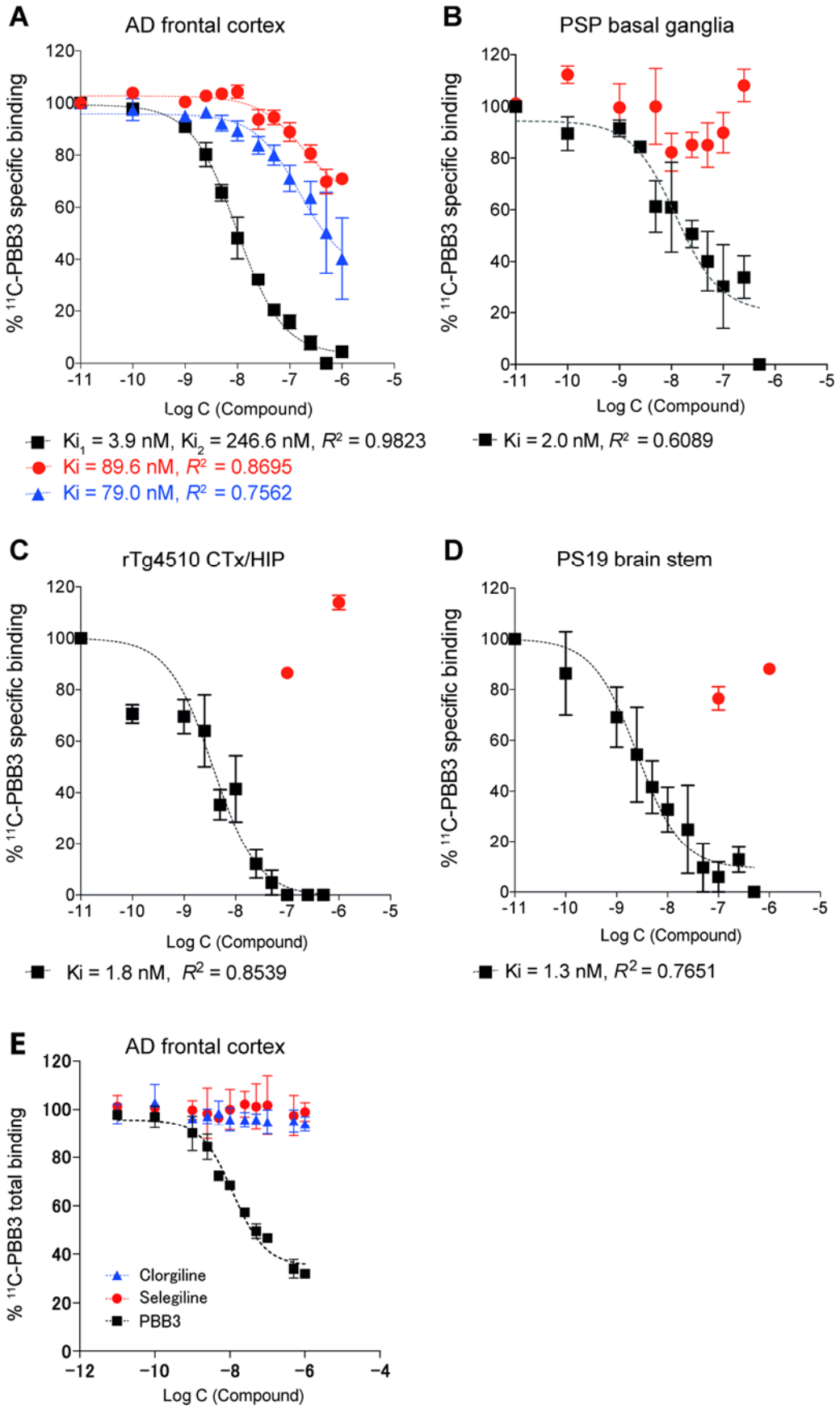

Figure 3 Assays of ^{11}C-PBB3 binding in the brain tissues derived from mouse models and AD patient

Specific binding of ^{11}C-PBB3 (5 nM) in the frontal cortex obtained from an AD patient (A), basal ganglia from a PSP patient (B), the neocortex/hippocampus of rTg4510 mice (C, mixture of samples derived from five mice undergoing PET scans), and brainstem/spinal cord from PS19 mice (D, mixture of samples derived from three 13-month-old mice). ^{11}C-PBB3 binding was blocked homologously by non-labeled PBB3 (black symbols) and heterologously by non-labeled AV-1451 (red symbols) and BTA-1 (blue symbols). Ki values were determined as described in Supplementary Materials and Methods. No notable displacement of ^{11}C-PBB3 binding by clorgyline or selegiline was observed in the frontal cortex of AD, in contrast to a significant blockade of the radioligand binding by unlabeled PBB3 (E). Data were generated from more than three independent experiments.

SUPPLEMENTARY INFORMATION

Comparative *in-vitro* and *in-vivo* quantifications of pathological tau deposits and their association with neurodegeneration in tauopathy mouse models

Ruiqing Ni[1, 2], Bin Ji[1*], Maiko Ono[1], Naruhiko Sahara[1], Ming-Rong Zhang[1], Ichio Aoki[1], Agneta Nordberg[2], Tetsuya Suhara[1] and Makoto Higuchi[1]

[1]National Institute of Radiological Sciences, National Institutes for Quantum and Radiological Science and Technology, Chiba, Chiba 263-8555, Japan; [2]Division of Alzheimer Research Center, Department of Neurobiology, Care Sciences and Society, Karolinska Institutet, Stockholm 14157, Sweden

[*]Corresponding Author: Bin Ji, Ph. D.

SUPPLEMENTARY MATERIAL AND METHODS

Animal Models

PS19 Tg mice heterozygous for human T34 (4RT isoform with a single N-terminal insert) with P301S mutation driven by the mouse prion protein promoter (*1*), were provided by the Perelman School of Medicine, University of Pennsylvania, and were bred and kept on a C57BL/6 background. rTg4510 mice, tau responder mice, and tetracycline-controlled transactivator (tTA) mice were obtained from the University of Florida. A parental mutant tau responder line on an FVB/N strain (Clea Inc., Osaka, Japan) and a tTA activator line in a 129+ter/SV strain (Clea Inc.) were generated and maintained. To generate a tau responder line expressing human T43 (4RT isoform without N-terminal inserts) with P301L mutation,

cDNA was placed downstream to a tetracycline-operon-responder construct. The tTA system was inserted downstream to the Ca^{2+}-calmodulin kinase IIα promoter. Hemizygous mice from each parental line were cross-bred to produce rTg4510 mice possessing both responding and tTA constructs and non-transgenic (non-Tg) littermates (*2*). A workflow of *in-vivo* PET and MRI and *in-vitro* binding assays with rTg4510 and non-Tg mice is shown in Supplemental Fig. 1.

Radiosynthesis and Small-animal PET Imaging

Radiosynthesis of ^{11}C-PBB3 was performed as described (*3*), and the resulting radiochemical purity was > 90 %. The molar activity of ^{11}C-PBB3 was 78-93.1 GBq/μmol at the end of synthesis. PET scans were performed by microPET Focus 220 animal scanner (Siemens Medical Solutions, Malvern, PA, USA) as described (*4*). At 7-10 months of age, rTg4510 mice (n = 5, body weight: 23.6 ± 0.8 g) and age-matched non-Tg mice (n = 7, body weight: 29.1 ± 1.5 g) were anesthetized with 1.5 % (v/v) isoflurane. Emission scans were acquired for 60 min in 3D-list-mode with an energy window of 350-750 keV, immediately after intravenous injection of ^{11}C-PBB3 (18.2-23.4 MBq/mouse; 20.76 ± 2.21 MBq for non-Tg and 21.24 ± 1.24 MBq for Tg mice). Images were reconstructed by either maximum-a-posteriori method to generate single-frame average images for non-quantitative displays or filtered back-projection using a 0.5-mm Hanning filter to generate dynamic images for quantitative assays. All Tg and four non-Tg mice were scanned by T_2-weighted MRI within one week of PET scans. Volumes of interest (VOIs) were placed on multiple anatomical structures, including the neocortex (coronal sections from 1.3 mm anterior to 2.7 mm

posterior to the bregma), whole hippocampus, cerebellum (6.4 to 7.0 mm posterior to the bregma) using PMOD® image analysis software (PMOD Technologies LLC, Zurich, Switzerland) with reference to individual T_2-weighted MRI for all Tg and four non-Tg mice or a brain template generated as described previously (*3*) for the other three non-Tg mice (Fig. 1A and Supplemental Fig. 2). The PET VOIs did not contain areas in the vicinity of the olfactory bulbs to circumvent radioactivity spillover from the Harderian glands. The neocotex more than 2.7 mm posterior to the bregma was excluded from the PET VOIs, since profound atrophy of this region in an aged rTg4510 mouse caused a partial volume effect on PET data, impeding an accurate quantification of the radioligand retention. Tracer uptake in each VOI was estimated as a percentage of injected-dose-per-tissue-volume (%ID/mL), which was uncorrected for body weights of animals, since changes of body weights during aging may not be necessarily proportional to alterations of brain weights. Non-displaceable binding potential (BP_{ND}) for ^{11}C-PBB3 binding in these VOIs, which is not influenced by either body or brain weights, was quantified with PMOD based on a simplified reference tissue model using the cerebellum as a reference region lacking tau deposits.

MRI of Mouse Brains

The rTg4510 mice were anesthetized with 1.5 % (v/v) isoflurane. T_2-weighted 2D multi-slice spin-echo (rapid acquisition with relaxation enhancement; RARE) was applied to the mouse heads using the 7.0-Tesla MRI system (Bruker BioSpin, AVANCE-III, Ettlingen, Germany) with a volume coil for transmission (Bruker BioSpin) and a quadrature surface coil for reception (Rapid Biomedical, Rimpar, Germany) with: repetition time (TR) = 4200 ms,

effective echo time (TE) = 36 ms, field of view (FOV) = 25.6×14.5 mm^2, slice thickness = 0.5 mm, number of slices = 28 (gapless), matrix = 256×256, RARE factor = 8, number of acquisitions (NA) = 8, norminal in-plane resolution = 100×57 μm^2. VOIs across all slices of the hippocampus and cortex were manually drawn with reference to Paxinos and Franklin's Mouse Brain Atlas using PMOD software.

In-vitro ^{11}C-PBB3 Binding Assays

All rTg4510 and non-Tg mice were killed by cervical dislocation after the scans. Brains were sampled from three PS19 and three non-Tg littermate mice at 13-months of age. The mouse brains were removed and divided into right and left hemispheres. The right hemispheres were kept at -80 °C for postmortem analyses, and the left hemispheres were fixed with 4 % paraformaldehyde in phosphate buffer overnight, followed by 30 % sucrose in phosphate buffer. Brain tissue from patients with AD and PSP were homogenized using MicroSmash (MS-100R; TOMY Digital Biology, Tokyo, Japan) in 50 mM Tris-HCl buffer (pH 7.4) containing a protease/phosphatase inhibitor cocktail (cOmplete™; Sigma-Aldrich). Concentrations of proteins in the brain homogenates were measured by BCA assays (Thermo Fisher Scientific). Aliquots of the homogenates were stored at -80 °C until the experiment.

Measurement of radioligand binding was performed by incubating 5 nM ^{11}C-PBB3 with brain tissue homogenates from five rTg4510 and seven non-Tg littermate mice undergone a PET scan, as well as from three PS19 mice and three non-Tg littermates. Non-specific binding was determined in the presence of 5×10^{-7} M unlabelled PBB3.

Homologous and heterologous competitive binding assays were performed: 100 µl

aliquots of the tissue homogenates containing 100 µg of AD brain tissue or 300 µg of mouse brain tissue were reacted with 900 µl of 50 mM Tris-HCl buffer (pH 7.4) containing 10 % ethanol, 5 nM ^{11}C-PBB3 in the presence of various unlabeled compounds including PBB3, BTA-1, AV-1451, clorgyline and selegiline at concentrations ranging from 10^{-11}-10^{-6} M for 30 min at room temperature in a dimly lit room to avoid photo-isomerization of the compound. Non-specific radioligand binding was determined in the presence of 5×10^{-7} M PBB3. Samples were run in duplicates, and the specific radioligand binding was expressed as pmol/g tissue.

The inhibitory constant (K_i), which is equivalent to the dissociation constant (K_D) in the homologous blocking assay, and the percentage of displacement were determined by using non-linear regression one-site and two-site binding models derived from the Cheng-Prusoff equation in GraphPad Prism version 5.0 (GraphPad Software, La Jolla, CA, USA), followed by F-test for model selection.

Immunohistochemical and Histochemical Analyses

Ten-µm-thick frozen sections from left hemispheres were generated in a cryostat (HM560; Carl Zeiss, Oberkochen, Germany) and used for immunostaining with an antibody against phosphorylated tau (AT8; 1:250 dilution) by following a standard immunohistochemical procedure described in our previous publications (*5*). Fluorescence microscopic visualization of tau fibrils with PBB3 and FSB was performed as described previously (*3*). All stained samples were examined by an all-in-one fluorescence microscope (BZ-9000; Keyence, Osaka, Japan), capable of tiling photomicrographs and merging them into a high-resolution

image with a large FOV.

References

1. Yoshiyama Y, Higuchi M, Zhang B, et al. Synapse loss and microglial activation precede tangles in a P301S tauopathy mouse model. *Neuron.* 2007;53:337-351.

2. Santacruz K, Lewis J, Spires T, et al. Tau suppression in a neurodegenerative mouse model improves memory function. *Science.* 2005;309:476-481.

3. Maruyama M, Shimada H, Suhara T, et al. Imaging of tau pathology in a tauopathy mouse model and in Alzheimer patients compared to normal controls. *Neuron.* 2013;79:1094-1108.

4. Ji B, Maeda J, Sawada M, et al. Imaging of peripheral benzodiazepine receptor expression as biomarkers of detrimental versus beneficial glial responses in mouse models of Alzheimer's and other CNS pathologies. *J Neurosci.* 2008;28:12255-12267.

5. Maeda J, Zhang MR, Okauchi T, et al. In Vivo Positron Emission Tomographic Imaging of Glial Responses to Amyloid-{beta} and Tau Pathologies in Mouse Models of Alzheimer's Disease and Related Disorders. *J Neurosci.* 2011;31:4720-4730.

SUPPLEMENTAL FIGURES

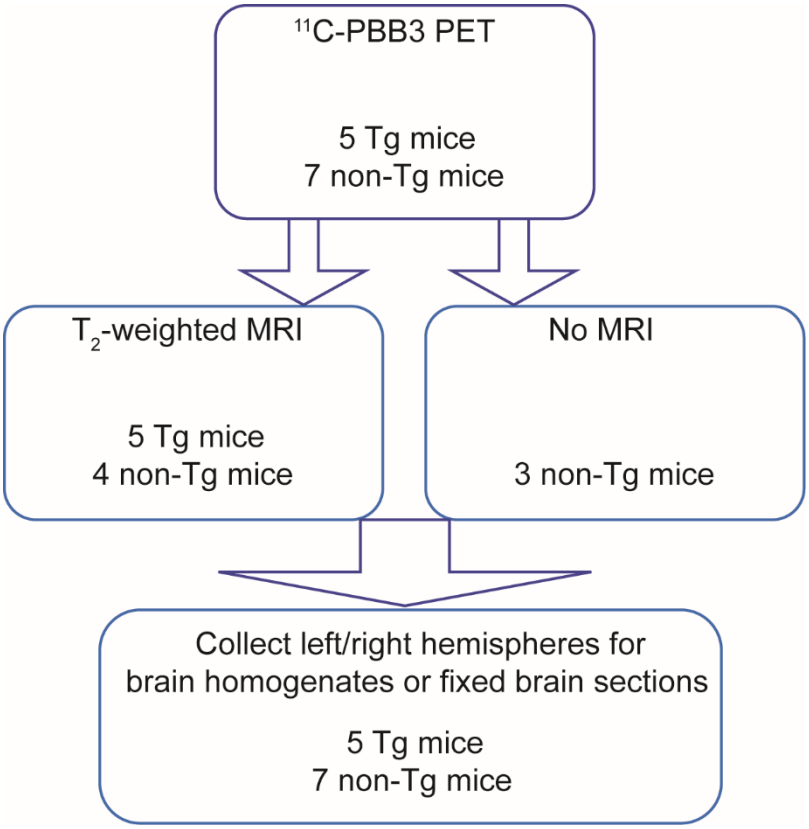

Supplemental Figure 1 (SFig. 1) Workflow of the current experiments using rTg4510 and non-Tg control mice. *In-vivo* ^{11}C-PBB3-PET for all Tg and non-Tg mice was followed by structural MRI for a subset of these animals. Brain samples of all mice were then collected for *in-vitro* ^{11}C-PBB3 binding assays and immunohistochemical analysis.

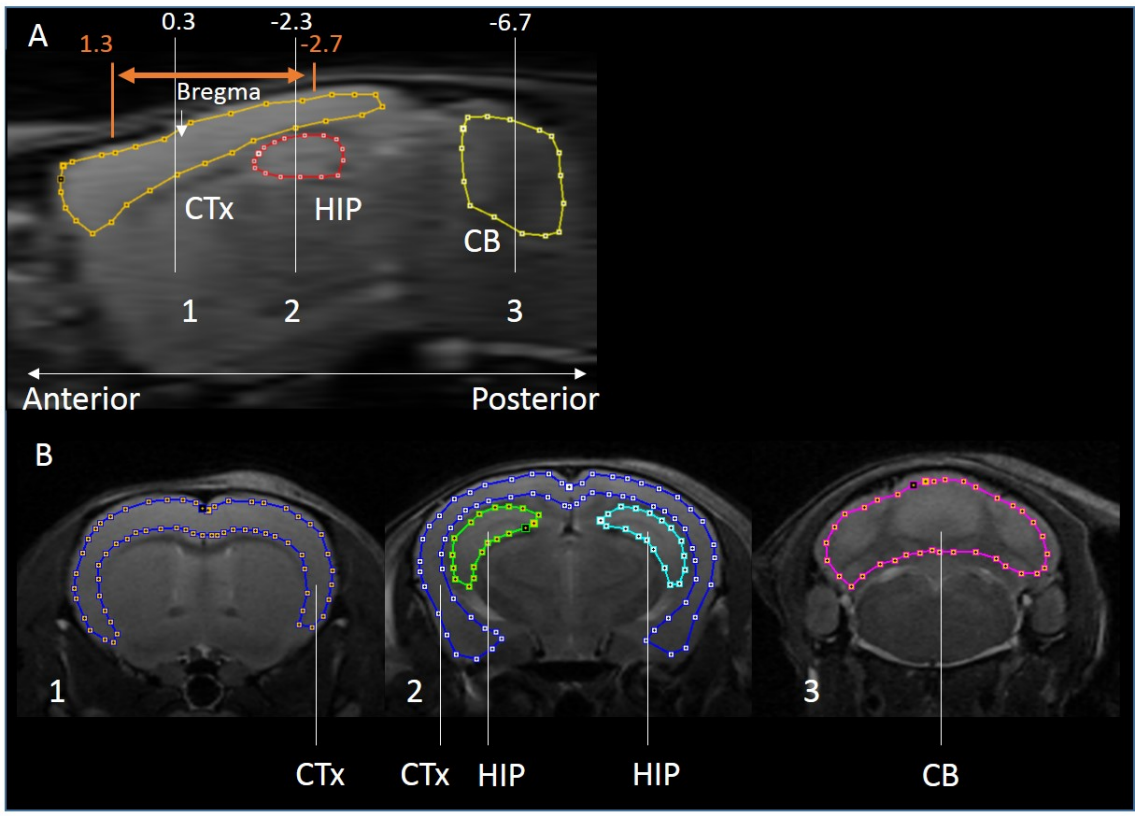

SFig. 2. Anatomical location of volumes of interest (VOIs) for PET and volumetric analysis.

Sagittal (A; 2.3 mm lateral to the bregma) T2-weight MRI slices of a non-Tg littermate of rTg4510 mouse showed ranges of three structures: neocortex (CTx), hippocampus (HIP) and cerebellum (CB). Representative VOIs on coronal section images at positions 1, 2 and 3 (0.3 mm anterior and 2.3 and 6.7 mm posterior to the bregma, respectively) were displayed in panel B. VOI covering the entire neocortex was used for the volumetric analysis, while the neocortical VOI used for PET measurements spanned from 1.3 mm anterior to 2.7 mm posterior to the bregma (indicated by an orange arrow).

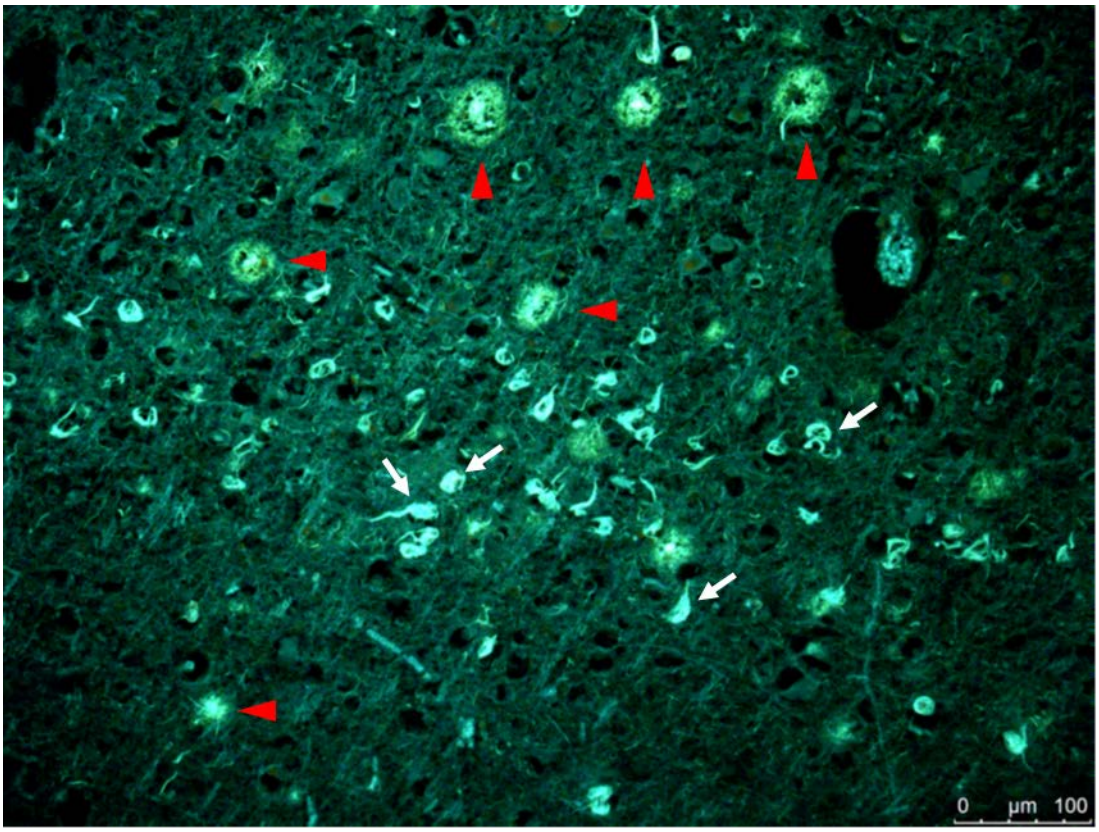

SFig.3. Fluorescent staining of an AD frontal cortex section with FSB. The tissue was derived from the region used for the homogenate binding assay. Amyloid plaques and neurofibrillary tangles were indicated by red arrowheads and while arrows, respectively.

The Journal of NUCLEAR MEDICINE

Comparative in-vitro and in-vivo quantifications of pathological tau deposits and their association with neurodegeneration in tauopathy mouse models

Ruiqing Ni, Bin Ji, Maiko Ono, Naruhiko Sahara, Ming-Rong Zhang, Ichio Aoki, Agneta Nordberg, Tetsuya Suhara and Makoto Higuchi

J Nucl Med.
Published online: February 1, 2018.
Doi: 10.2967/jnumed.117.201632

The Journal of Nuclear Medicine is published monthly.
SNMMI | Society of Nuclear Medicine and Molecular Imaging
1850 Samuel Morse Drive, Reston, VA 20190.
(Print ISSN: 0161-5505, Online ISSN: 2159-662X)

SNMMI SOCIETY OF NUCLEAR MEDICINE AND MOLECULAR IMAGING